

High Performance of Porous, Hierarchically Structured P2- $\text{Na}_{0.6}\text{Al}_{0.11-x}\text{Ni}_{0.22-y}\text{Fe}_{x+y}\text{Mn}_{0.66}\text{O}_2$ Cathode Materials

Marius Schmidt, Valeriu Mereacre, Holger Geßwein, Nicole Bohn, Sylvio Indris, and Joachim R. Binder*

Sodium-ion-batteries (SIB) are a low-cost alternative to currently used lithium-ion batteries (LIB) but suffer from poor cycling stability. Spray drying provides porous, hierarchically structured particles of cathode active material (CAM) in large amounts, suitable for up-scaling. Changing the chemical composition of the $\text{Na}_{0.6}\text{Al}_{0.11-x}\text{Ni}_{0.22-y}\text{Fe}_{x+y}\text{Mn}_{0.66}\text{O}_2$ layered oxides under identical synthesis conditions lead to differences in particle morphology, conductivities, sodium vacancy ordering, and phase transition, therefore influencing the electrochemical performance via several mechanisms. Here, a broad overview on these changes for samples with variable nickel and iron content is presented. With increasing iron content, the particle porosity is reduced and lower initial capacity is received for most cycling windows. Substituting half of the original Ni amount with Fe still leads to high capacities and improved cycling stability. The influence of Al as electrochemically inactive element becomes visible in stabilized cycling stability as well.

will climb to a level considerably beyond supply output in the following decades until 2050. This analysis shows that the price of either of the two elements, as well as any battery system based on them, will rise significantly over the next few decades. Sodium, magnesium, and aluminium are lithium-alternative elements for energy storage and are by three orders of magnitude more abundant in the earth's crust.^[4] Their energy storage mechanisms have already been investigated in battery systems.^[5,6] Among these post-lithium systems sodium-ion-batteries are the closest to commercialisation,^[7] demonstrated by various companies.^[8] They will not completely replace LIBs, but rather more SIBs are thought to be a promising and cost-effective alternative battery

1. Introduction

More improvements in energy storage technologies are required to address global challenges such as the decrease of greenhouse gases. The electrification of the transport sector exhibits a potential of reducing emissions and large-scale stationary storage is regarded as a crucial technology to smooth the fluctuations of renewable energies in the power grid.^[1] Besides high energy density and safety precautions, the cost of battery cells is a key factor in battery development.^[2] As we move toward sustainable energy, there is a rising need for energy storage technology. Vaalma et al.^[3] forecast in their work from 2018 that the demand for lithium and cobalt induced by the global battery industry alone

technology. Moreover, it should be mentioned, that copper foil is not required for SIBs as a current collector. On both electrodes, aluminium, which is the third-most abundant material in the continental crust of the earth, can be employed as an inexpensive current collector.^[3,5]

Layered oxides are a promising candidate for SIB cathode active material (CAM). They are known for their high specific capacity and high average operating voltage. However, capacity fading presents a problem for their application. Irreversible capacity loss can result from a variety of degradation mechanisms, such as severe volume change of the crystal structure, which can lead to loss of contact^[9] and phase transitions at voltages beyond 4.1V.^[10] These phase transitions may involve the oxidation of oxygen from the lattice.^[11] The crystal structure consists of transition metal (TM) layers, just like their LIB counterparts. These layers are capable of intercalating Li and Na ions. Many TMs, including Mn, Fe, Co, and Ni, as well as combinations of them, have been studied and have an impact on the electrochemical performance.^[12] Two primary groups of the layered oxides that can be distinguished are P2-type and O3-type layered oxides, in which the environment of the sodium ion is either prismatic or octahedral. The number of non-equivalent TM layers are represented by the integers two and three.^[13] Typically temperatures between 650 and 900°C and a sodium content of $0.3 \leq x \leq 0.7$ (Na_xTMO_2) lead to the formation of P2-type layered oxides.^[14] The lack of sodium in P2-type materials is a drawback, since it results in reduced capacity in full cells. Pre-sodiation of electrodes

M. Schmidt, V. Mereacre, H. Geßwein, N. Bohn, S. Indris, J. R. Binder
Institute for Applied Materials
Karlsruhe Institute of Technology
Hermann-von-Helmholtz-Platz 1, 76344 Eggenstein-Leopoldshafen,
Germany
E-mail: joachim.binder@kit.edu

The ORCID identification number(s) for the author(s) of this article can be found under <https://doi.org/10.1002/aenm.202301854>

© 2024 The Authors. Advanced Energy Materials published by Wiley-VCH GmbH. This is an open access article under the terms of the Creative Commons Attribution-NonCommercial-NoDerivs License, which permits use and distribution in any medium, provided the original work is properly cited, the use is non-commercial and no modifications or adaptations are made.

DOI: 10.1002/aenm.202301854

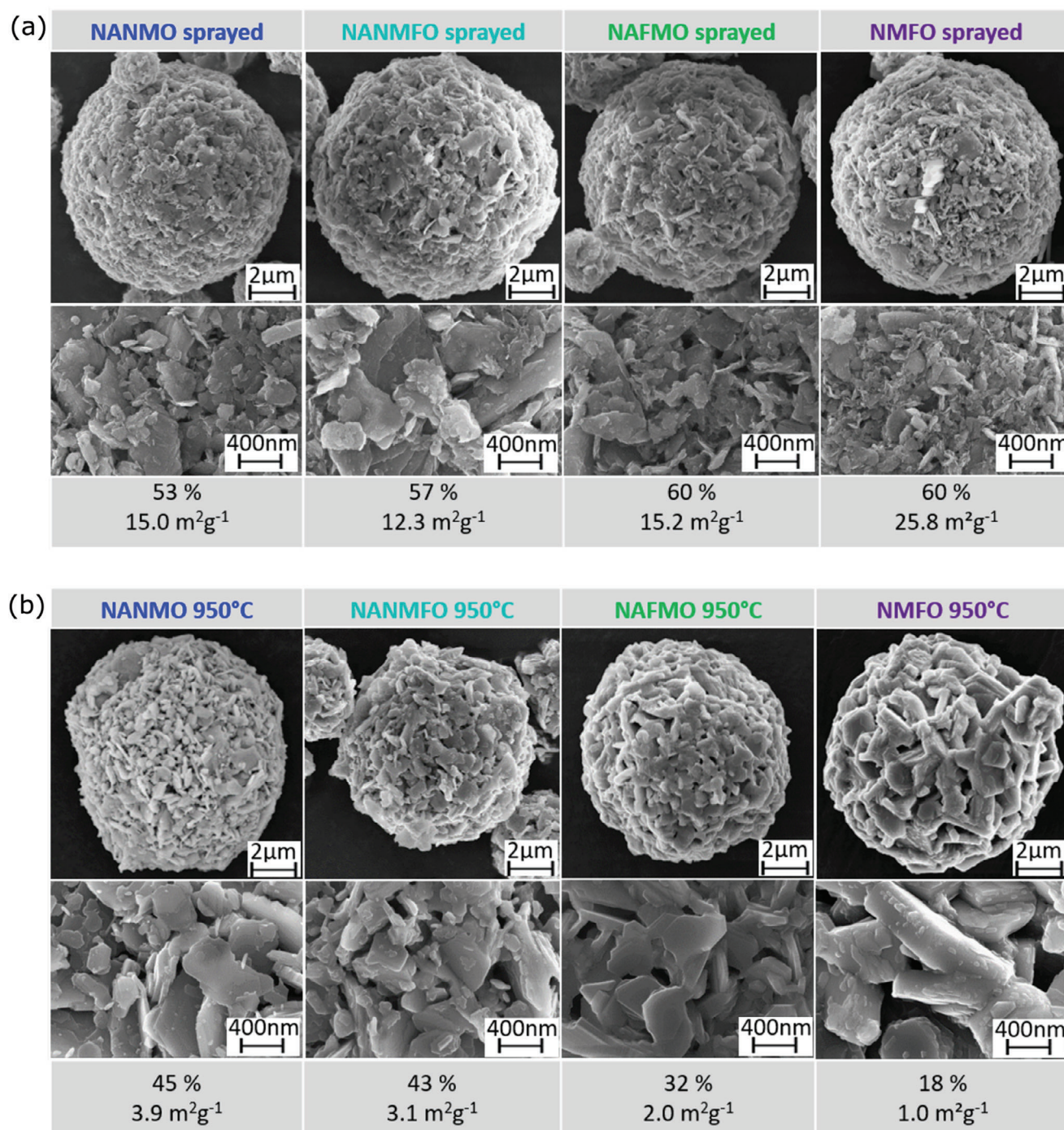


Figure 1. Particle morphology: SEM micrographs reveal the morphology of the active material. The secondary particles are shown in (a) after spray drying and in (b) after sintering with $T_S = 950^\circ\text{C}$. Particle porosity Φ in % and specific surface area A_{BET} in $\text{m}^2 \text{g}^{-1}$ supplement the SEM pictures.

may be able to resolve this problem, but poses another challenge in the preparation.^[15] There are two possible sites for Na ions in the prismatic (P-type) environment. Because of the large ionic radius of Na^+ , adjacent prismatic Na_e (edge sharing) and Na_f (face sharing) sites cannot be occupied at the same time.^[12] Therefore, sodium ion vacancies in the structure are created. An ordered intermediate phase results from ordering of these vacancies. Sev-

eral voltage plateaus and diffusion barriers appear when this order is changed during charge and discharge. Absence of distinct plateaus suggests a solid-solution reaction free of a superstructure and therefore with lowered sodium diffusion barriers.

Substitution of different TMs or electrochemically inactive metals such as Mg or Al into the layered structure can lead to a smoothing of these plateaus and can improve battery

performance at higher C-rates,^[16] as well as rate stability.^[17] The right combination of different metals can be understood as engineering toward optimised properties. Fu et al.^[18] demonstrated that the use of electrochemically inactive Mg or Ca individually can improve the lattice stability of a P2-type Ni-Mn-based layered oxide. However, it was also observed that the Ca-substituted material showed unwanted side-reactions in the high voltage region. This disadvantage could be reduced when small amounts of magnesium were added to the chemical composition, demonstrating a synergetic effect of the Mg/Ca co-substitution.

Cathode active materials with an engineered microstructure consisting of nanosized particles have been demonstrated to be an effective way to boost initial specific capacity and improve capacity retention after cycling in LIB and SIB systems.^[19,20] Ren et al.^[20] created nanofiber SIB cathode material with the electrospinning method and achieved remarkable cycling stability over 10,000 cycles with high rate. However, the industrial application of electrospinning is limited due to the low production rate of material.^[21] Another approach was chosen by Wagner et al.,^[19] who proposed a spray drying technique to synthesise CAMs with a hierarchical structure of spherical (secondary) particles composed of nanosized (primary) particles. This spray drying technique produces micrometer sized CAM powders with a high tap density and is suitable for up-scaling toward industrial production.^[22]

In this work, we present the synthesis, structural and electrochemical characterization of four different P2-type cathode materials for SIBs with a hierarchical microstructure. Starting point is the nickel containing $\text{Na}_{0.6}\text{Al}_{0.11}\text{Ni}_{0.22}\text{Mn}_{0.66}\text{O}_2$ (NANMO), inspired from the work of Hasa et al.^[23] Here, aluminium acts as inactive component for better cycling stability. Due to the toxicity of nickel and being a major cost driver for battery materials, a sustainable battery chemistry with this element is questionable.^[2,24] Therefore, nickel is gradually replaced with non-toxic and low cost iron to receive $\text{Na}_{0.6}\text{Al}_{0.11}\text{Ni}_{0.11}\text{Mn}_{0.66}\text{Fe}_{0.11}\text{O}_2$ (NANMFO) and $\text{Na}_{0.6}\text{Al}_{0.11}\text{Fe}_{0.22}\text{Mn}_{0.66}\text{O}_2$ (NAFMO). Finally, the electrochemically inactive element aluminium is also substituted with iron, which yields a composition of $\text{Na}_{0.6}\text{Mn}_{2/3}\text{Fe}_{1/3}\text{O}_2$ (NMFO).

2. Results and Discussion

2.1. Chemical Composition and Particle Morphology

The obtained chemical composition was controlled after the final heat treatment with ICP-OES. Only less than 0.4 wt% of residual carbon remain after the final heat treatment with a sintering temperature $T_s = 950^\circ\text{C}$ in air atmosphere. The other elements are in good agreement with the nominal values and are summarized in the Supporting Information (Table S1, Supporting Information). The primary particles of the synthesized CAM samples after the ball milling process show a broad size distribution between 0.2 and $10\mu\text{m}$ as determined by laser light scattering. The average primary particle sizes are 1.67, 1.65, 1.42, and $1.11\mu\text{m}$ for NANMO, NANMFO, NAFMO, and NMFO, respectively. After spray drying these primary particles are agglomerated into porous, spherical granules with sizes ranging between 3 and $30\mu\text{m}$. An overview of the particle sizes can be found in Table S2 (Supporting Information). The porosity of the granules lies between 53% and 60%, whereas a general trend can be observed,

that the iron containing samples exhibit higher porosities. The BET specific surface area shows similar values for the four materials (12.3 to $15.2\text{m}^2\text{g}^{-1}$) except for NMFO with a high value of $25.8\text{m}^2\text{g}^{-1}$. This high surface area and the smallest observed primary particle size for NMFO indicates that the ball milling process was most effective for this CAM. SEM micro graphs of the spray dried CAM granules are presented in Figure 1a, which show the hierarchical micro-structure of the samples. The grain sizes seen by SEM are in the order of some hundred nano meters, which demonstrates that the average primary particles measured with light scattering are actually several agglomerated crystallites. Sintering at 950°C changes the micro-structure of the CAM granules. It can be seen, that the porosity, specific surface area, as well as the surface roughness have decreased during this heat treatment. The primary particles receive a flake-like shape and the secondary particles maintain their spherical appearance. The CAM with the highest nickel content exhibits the highest porosity and surface area, whereas with increasing iron content these values decrease from NANMO to NMFO (see Figure 1b). The high surface area of NMFO results in a high sinter activity and drives the densification during the calcination process, leading to very dense granules with a low porosity of only 18%. Compared to the iron free material NANMO the iron containing samples all show an increased densification behavior with lower porosity values of the spherical granules, which indicates that a higher iron content is beneficial for the sinter activity of these CAMs and that iron enhances grain growth, as can be seen from the SEM images in Figure 1b.

In Figure 2 the micro structure inside the particles is revealed with SEM cross sections of cathodes. It can be seen that the spherical secondary particles are porous, which allows an electrolyte penetration inside of all CAMs. The cross-section images are in good agreement with the porosity data of sintered secondary particles (see. Table S2, Supporting Information): Porosity Φ decreases from NANMO (highest nickel content) to NMFO (highest iron content), while the primary particle size is increasing. The reason for that is the above described sinter activity due to the presence of iron.

2.2. Ex Situ XRD

Ex situ XRD measurements were performed after the final synthesis with the sintering temperature of 950°C . Figure 3 shows the XRD patterns together with the Rietveld refinement results of the four different chemical compositions. To limit the number of refined parameters, stoichiometry constraints according to the ICP-OES results, i.e., the sum of the TMs fractions was set to 1 and the sodium fraction was 0.6, were used. All materials crystallize as layered oxides in the ideal P2 structure with hexagonal space group $P6_3/mmc$. The refined lattice parameters for NANMO are $a = 2.8631(4)\text{\AA}$ and $c = 11.2352(4)\text{\AA}$. The gradual substitution of large Fe^{3+} ions (radius 0.65\AA) into the crystal structure leads to an increase of the lattice parameters with increasing Fe content in the order NANMFO ($a = 2.8746(3)\text{\AA}$ and $c = 11.2587(3)\text{\AA}$), NAFMO ($a = 2.8829(6)\text{\AA}$ and $c = 11.2843(4)\text{\AA}$) and NMFO ($a = 2.9163(3)\text{\AA}$ and $c = 11.2982(2)\text{\AA}$). The diffraction profiles of all synthesized materials exhibit anisotropic, hkl-dependent peak broadening, i.e. the 10l

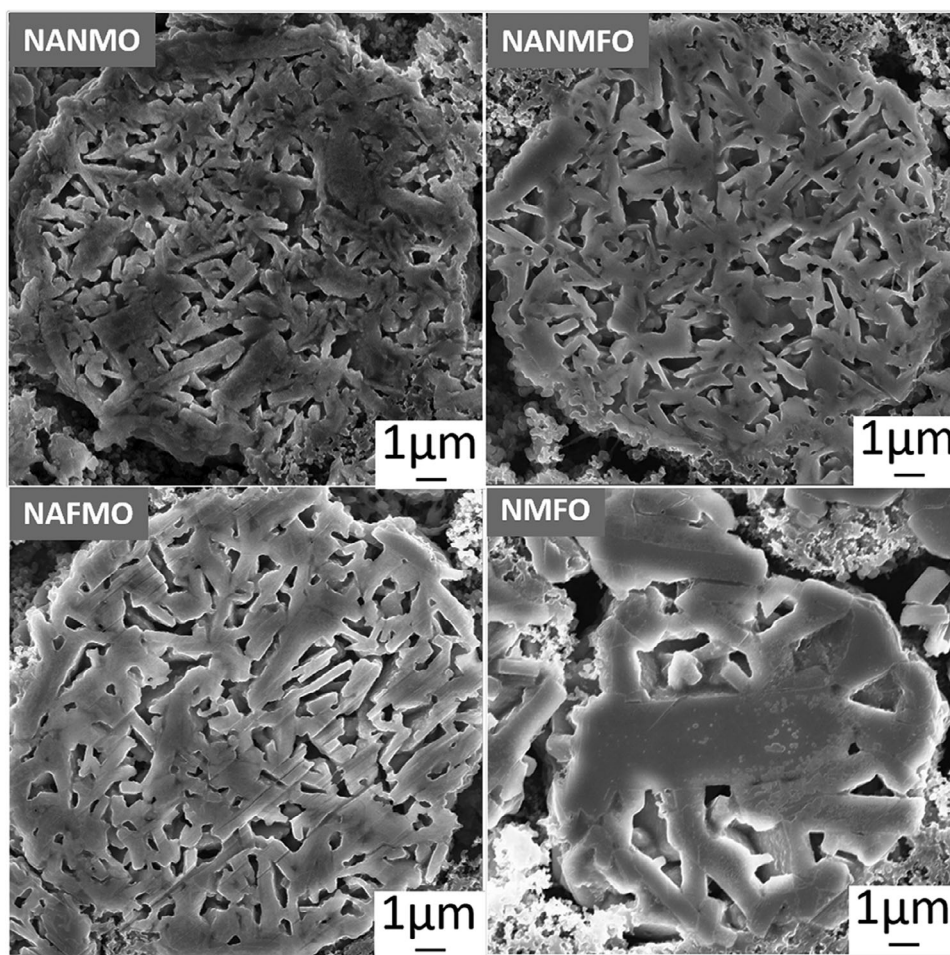


Figure 2. Electrode cross section: Ion-etched cathodes reveal the inter granular porosity of secondary particles. As presented with Hg-porosimetry data in Table S2 (Supporting Information) the porosity decreases from highest nickel content (NANMO) to highest iron content (NMFO).

reflections are broader than the 00l and hk0 reflections. This kind of microstructural induced peak broadening hints to the presence of stacking faults, which was also reported earlier for layered P2-type sodium ion CAMs.^[25,26] Therefore, during Rietveld refinements, profile broadening was accounted for by the use of a crystallite size broadening function together with the phenomenological anisotropic strain broadening model of Stephens.^[27] The Stephens model improved the fitting quality of the profile shapes, but some discrepancies still exist. The volume average column lengths were estimated based on a double Voigt approach as implemented in the Topas software. For NANMO this value was calculated to approximately 67Å. The domain sizes for the iron containing materials are ≈61Å for NANMFO, ≈43Å for NAFMO and ≈65Å for NMFO. The largest observed crystallite size for NMFO is in accordance with the SEM investigations and underlines the increased crystal growth as the iron content is increased.

In case of NANMO minor additional reflections were present in the diffraction pattern. These reflections can be indexed with the acentric hexagonal space group $R3m$ derived from the $AlCuO_2$ structure^[28] and correspond to an impurity phase, most

likely an O3-type layered oxide. The specific chemical composition of the impurity is unknown. For NANMFO the same reflections with less intensity are visible, while NAFMO exhibits no additional reflections. With the presence of an impurity phase, the sintering temperature $T_s = 950^\circ\text{C}$ can be interpreted as non-optimal. More homogeneity of the desired P2-type phase can in general be achieved with higher sintering temperatures. It was described before that the sinter activity is increasing with the iron content. Since more iron leads to a better diffusion of sintering particles a better homogeneity and therefore less impurity can be expected. This was supported by further experiments, which will be published subsequently, that showed that the impurity phase vanished for NANMFO at higher sintering temperatures, while for NANMO it was almost not visible anymore. In the presented work $T_s = 950^\circ\text{C}$ was chosen as a compromise in order to compare all four materials after the same synthesis process. NMFO is nearly phase pure. Only very weak reflections of a different impurity phase isostructural to $MnFe_2O_4$ spinel^[29] are visible in the diffraction pattern. A summary of the refined crystallographic parameters can be found in the Supporting Information.

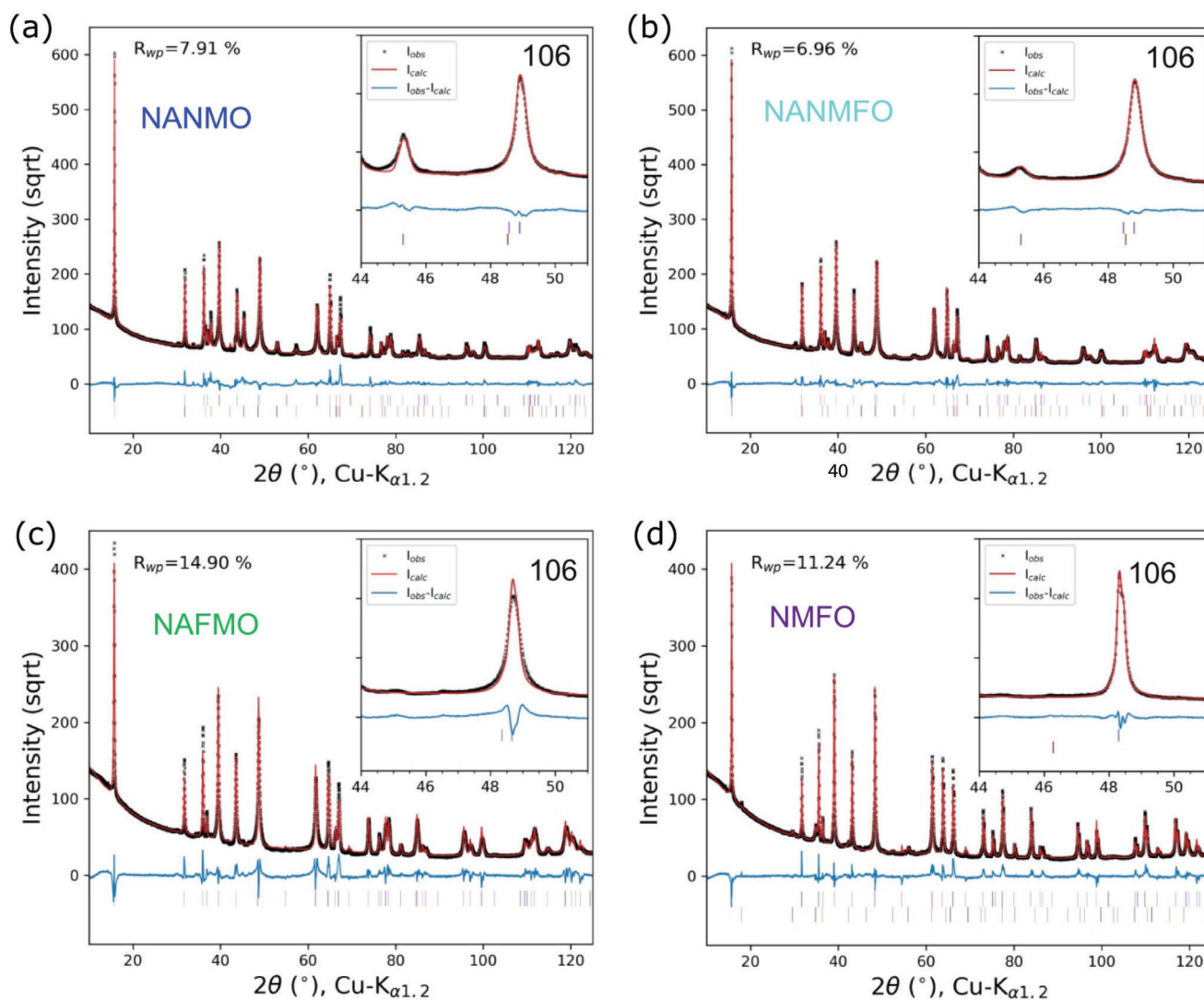


Figure 3. X-ray diffraction patterns and Rietveld refinement of a) NANMO, b) NANMFO, c) NAFMO, and d) NMFO materials sintered at 950 °C. NANMO and NANMFO contain small amounts of an impurity phase with hexagonal R3m structure (lower tics), whereas NMFO shows very weak reflections of a MnFe_2O_4 spinel phase (lower tics).

2.3. Mössbauer Spectroscopy

The chemical compositions of the four cathode materials were chosen to investigate the influence of the substitution of Al and Ni for Fe on the materials' properties. Ni is considered to be a cost driver of battery materials^[2] while Fe is one inexpensive option to replace it. In P2-type oxides, the process of $\text{Ni}^{3+} / \text{Ni}^{4+}$ oxidation/reduction takes place at around 3.5 to 3.7 V (against $\text{Na}|\text{Na}^+$)^[23,30] and $\text{Fe}^{3+} / \text{Fe}^{4+}$ oxidation/reduction occurs at approx. 4.0 to 4.1 V.^[31] It is necessary to understand if and to what extend Fe is electrochemically active in these iron containing cathode materials in the different voltage regimes. Mössbauer spectroscopy was performed on the pristine materials after sintering at $T_s = 950$ °C, and after charging to 4.6 V. For the materials recovered after charging, thick cathode sheets were used (coated with 800 μm gap size, ca. four times higher mass loading compared to regular electrodes, for better signal inten-

sity). When the upper voltage limit was reached, the cell voltage was kept constant until the current was smaller than $C/50$ to ensure full charge. The cells were then opened in argon atmosphere, the cathodes were washed with dimethylcarbonate (DMC), and removed from the current collector. About 50 mg were recovered from two coin cells to achieve the desired sample mass.

While the spectra of the pristine materials show exclusively Fe^{3+} , the spectra of the samples obtained after charging to 4.6 V reveal a mixture of Fe^{3+} and Fe^{4+} , i. e., the partial oxidation of Fe^{3+} to Fe^{4+} during the charging process (Figure S1, Supporting Information). The fractions of Fe^{3+} and Fe^{4+} are determined from the area fractions of the corresponding doublets in the Mössbauer spectra and listed in in Table 1. The different samples show different degrees of Fe oxidation. A more effective Fe oxidation can certainly be achieved via higher upper cut-off voltage (but this might be detrimental to the electrochemical

Table 1. Iron oxidation states in the charged state (after charging to 4.6 V) as obtained from Mößbauer spectroscopy: the fractions of Fe³⁺ and Fe⁴⁺ were determined from the area fractions of the corresponding doublets in the Mößbauer spectra (Figure S1, Supporting Information).

NANMFO	Fe ³⁺	73.5%
	Fe ⁴⁺	26.5%
NAFMO	Fe ³⁺	62.6%
	Fe ⁴⁺	37.4%
NMFO	Fe ³⁺	68.0%
	Fe ⁴⁺	32.0%

performance), lower charging current, thinner electrodes, higher porosity of secondary particles, and smaller primary particles. The lowest amount of Fe⁴⁺ was measured for NANMFO. This cathode material still contains Ni that contributes to the specific capacity. For that reason, a low amount of Fe⁴⁺ is explainable. In the case of the nickel-free materials NAFMO and NMFO, a significantly higher Fe⁴⁺ fraction was detected. For NAFMO the highest amount of Fe⁴⁺ was measured, since this active material has a higher porosity of 32% after sintering at $T_S = 950^\circ\text{C}$, while for NMFO it is only 18%. In the SEM micrographs of cathode cross-sections (shown in Figure 2) it is also visible that NMFO exhibits bigger primary particles than NAFMO, which is also a reason for sluggish Fe³⁺ oxidation inside these particles. The before proposed mechanism between iron content and sinter activity results here in differently high amounts of Fe⁴⁺.

2.4. Conductivity

In general, a cathode material needs good ionic and electronic conductivity σ_j ($j = i, e$). These are fundamental and intrinsic properties of the cathode material.^[32] Only a few reports in the literature present intrinsic transport properties of active material without conductive carbon. The latter is added in the slurry preparation and improves the overall electronic conductivity of an electrode,^[33] but here we are interested in the conductivities of the pure cathode active material.

For NMC (lithium nickel-manganese-cobalt oxide) Zahnnow et al.^[32] investigated both the electronic and ionic conductivity. They suggested a physically meaningful equivalent circuit where the contributions of the two resistors R_e (electronic) and R_i (ionic) to the impedance were overlapping. In case of sodium-based layered oxides, only few reports can be found in the literature, such as the work from Walczak et al.^[34] where only the electronic conductivity was determined. In the present work, we suggest a combination of the two mentioned approaches (Walczak et al.^[34] and Zahnnow et al.^[32]): An investigation of a sodium-based layered oxides with the analysis method from Zahnnow et al.^[32] to determine the ionic part of the conductivity. However, the circuit model proposed by Zahnnow et al. had to be modified to be applicable in current case of a layered Na transition metal oxide.

A detailed description of the impedance spectra, the used equivalent circuit model, and its interpretation can be found in the Supporting Information. Performing these impedance measurements at various temperatures, one obtains the activation

energies for the electronic and ionic contributions, i. e., plotting $\log(\sigma_j T)$ versus reciprocal temperature in accordance with the Arrhenius law (Equation (1)) leads to linear plots (Figure 4).

$$\sigma = \frac{\sigma_0}{T} \cdot \exp\left(-\frac{E_A}{k_B T}\right) \quad (1)$$

As described in the previous sections, the following trend for the sintering activity was observed when comparing the four different chemical compositions. This activity increased when going from high nickel content to high iron content and A_{BET} and Φ were inversely proportional to this sintering activity. In case of the conductivities, such a trend is not visible. The conductivity is related to crystal structure and electronic band structure. Introducing substitutional elements may change the bandgap and therefore affect the electronic conductivity.^[35,36] The ionic conductivity is influenced by the concentration of charge carriers, their mobility, and their charge.^[37] In Table 2 the room temperature conductivities and activation energies E_{A_j} ($j = e, i$) for the transport mechanisms are summarized. The materials are sorted from highest Ni content to highest Fe content from top to bottom.

It is clear that, while NMFO displays the lowest values for both electronic and ionic conductivity, NANMO exhibits the highest values for both. Although the porosities of NANMO and NAFMO are just slightly different, their electronic and ionic conductivities differ by one and two orders of magnitude, respectively. Although it can be assumed that some of the variation of σ_j is caused by the various porosities, it is doubtful that this will cause the conductivity to alter by several orders of magnitude. Yet, while having different porosities, NANMFO and NAFMO show quite similar conductivities. So it can be assumed that the conductivities are not just a result of the samples' porosities but represent a material property. In a completely dense sintered sample without pores or grain boundaries the conductivities depend only on the chemical composition. It has been reported that the introduction of substitution ions (doping) can reduce more of the transition metal ions from their tetravalent state TM^{4+} into the trivalent state TM^{3+} .^[35] A mix of both valence states $\text{TM}^{4+}/\text{TM}^{3+}$ can lead to the formation of electron holes in the narrow $\text{TM}^{4+}/\text{TM}^{3+}$ band, which increases the conductivity.^[38] With Mößbauer spectroscopy it was demonstrated that exclusively Fe³⁺ was present in the iron containing CAMs. Unfortunately the same method could not be used to investigate iron free NANMO. It seems possible that Mn might exhibit a mix of valence states, since its transition of $\text{Mn}^{3+}/\text{Mn}^{4+}$ in half cells is located close to the open circuit voltage (synonymous to the pristine material investigated with EIS).^[39] That would also result in a mix of $\text{Ni}^{2+}/\text{Ni}^{3+}$ as well. The incorporation of Fe³⁺ would shift those ratios. That might explain the high electronic conductivity of NANMO. An example of how the chemical composition can influence the valence states is given by Carlier et al.^[40] for a Li-based layered oxide. They reported that Co^{3+} is less likely to be oxidized to Co^{4+} if nickel is present in the structure. On the other hand the diameter of substitutional elements can influence the lattice parameters and hence ionic diffusion in the lattice.^[35]

There are only few reports in literature about the conductivities of layered sodium oxides with comparable composition. Similar impedance measurements were conducted by Walczak et al.^[34] on

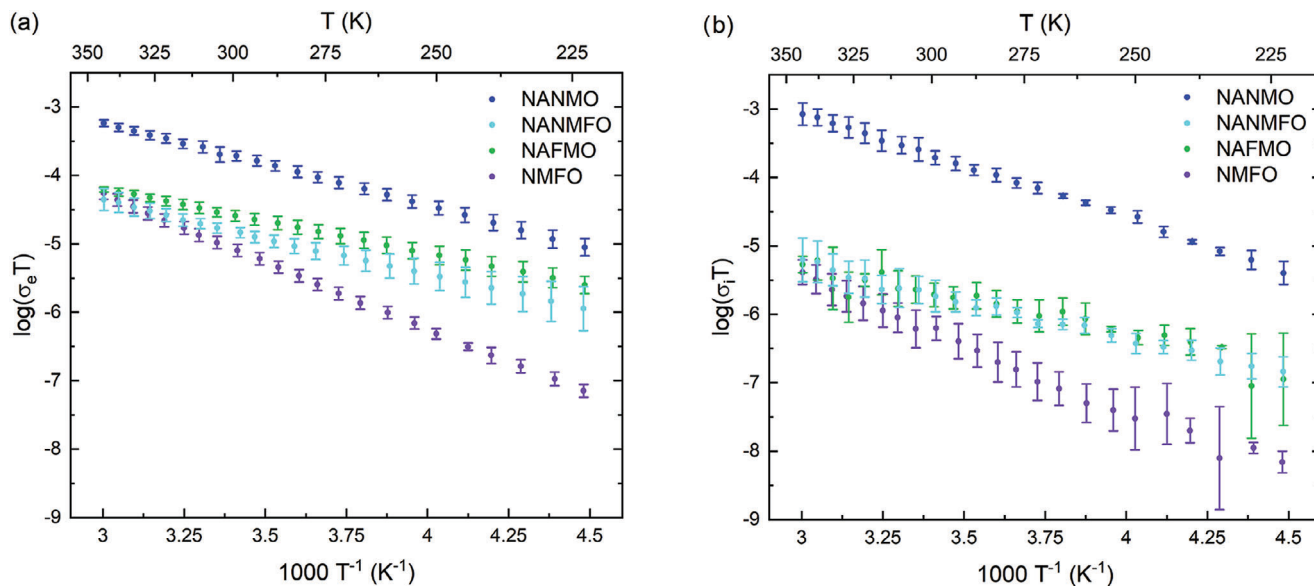


Figure 4. Arrhenius plots of a) electronic and b) ionic conductivity. The logarithm to the base ten was used for the plot for simple interpretation. Calculation of activation energies used natural logarithm.

$\text{Na}_{0.67}\text{Fe}_{0.5}\text{Mn}_{0.5}\text{O}_2$ and on $\text{Na}_{0.67}\text{Fe}_{0.2}\text{Mn}_{0.8}\text{O}_2$. They noticed compressed semicircles in the Nyquist plots similar to those observed for NMFO in Figure S4 (Supporting Information). However, they could not differentiate between ionic and electronic processes and derived their conductivities from the fit of two RQ-elements in series, which correspond to R_e according to Equation (S1) or (S3) (Supporting Information). The results published by Walczak et al. for the electronic activation energy E_{A_e} of 0.39 and 0.37 eV are comparable to the values found for NMFO in the presented investigation as well as for the other chemical compositions.

In Table 2 also room temperature conductivities are shown. In the work from Walczak et al.^[34] the composition with the highest iron content $\text{Na}_{0.67}\text{Fe}_{0.6}\text{Mn}_{0.4}\text{O}_2$ shows the lowest conductivity $\sigma_e = 5.78 \cdot 10^{-8} \text{ Scm}^{-1}$. This is in agreement with our data with $\sigma_e = 2.8 \cdot 10^{-8} \text{ Scm}^{-1}$ (NMFO, highest iron content) to $6.4 \cdot 10^{-7} \text{ Scm}^{-1}$ (NANMO, no iron content). It should be mentioned that Walczak et al. used $T_s = 800$ and 900 °C instead of 950 °C employed in this study, which is certainly a reason for the different value for NMFO. This also supports the previous idea that the ideal sintering temperature for NMFO and NAFMO is lower than 950 °C. Furthermore, Walczak et al. did not mention what pressing force was applied and what porosity the pellets exhibited after the sintering.

The activation energy for ionic hopping E_{A_i} and the ionic conductivity can be compared to the results for Li-NMC from Zahnw et al.^[32] They determined the activation energy for the ionic hopping process to be between 0.34 and 0.59 eV, which is nearly identical to their measured E_{A_e} . The same seems to be true for the four-layered sodium oxides, where both processes have similar activation energies. Different sintering temperatures and porosities were investigated by Zahnw et al. The values most similar to those of our investigations are $T_s = 950$ °C and $\Phi = 24\%$. Lithium-based NMC-pellets with these parameters exhibited $\sigma_e = 2.5 \cdot 10^{-8} \text{ Scm}^{-1}$ and $\sigma_i = 4.9 \cdot 10^{-8} \text{ Scm}^{-1}$, with both values in the same order of magnitude and $\sigma_e < \sigma_i$. In case of the sodium-based layered oxides this is only the case for NANMO. The other iron containing materials share the common feature that the ionic conductivity is approx. one order of magnitude smaller than the electronic one.

One feature of this data needs to be highlighted, because it will be relevant later again: Even though NANMO exhibits the highest ionic conductivity, the activation energy E_{A_i} of the ionic hopping process is higher than for NANMFO and NAFMO. Especially the difference between NANMO and NANMFO will become visible later in the in situ XRD data, as well as during electrochemical cycling.

Table 2. Activation energies E_{A_j} and electronic/ionic conductivities σ_j ($j = e, i$) at $T = 20$ °C. The average porosity Φ of the pellets differs slightly for the different materials.

Material	E_{A_e} in meV	E_{A_i} in meV	σ_e in Scm^{-1}	σ_i in Scm^{-1}	Φ in %
NANMO	241 ± 6	295 ± 19	$(6.4 \pm 0.5) \cdot 10^{-07}$	$(7.1 \pm 0.2) \cdot 10^{-07}$	22 ± 1
NANMFO	212 ± 52	215 ± 61	$(5.2 \pm 0.8) \cdot 10^{-08}$	$(6.8 \pm 1.7) \cdot 10^{-09}$	26 ± 1
NAFMO	187 ± 12	188 ± 12	$(9.0 \pm 1.3) \cdot 10^{-08}$	$(7.7 \pm 2.8) \cdot 10^{-09}$	20 ± 3
NMFO	390 ± 1	378 ± 13	$(2.8 \pm 0.4) \cdot 10^{-08}$	$(1.8 \pm 0.6) \cdot 10^{-09}$	24 ± 1

2.5. Operando XRD

The thicker cathodes used for the operando XRD study were pre-cycled with 1C and delivered approximately 78% to 88% of the specific capacity of thinner cathodes, which were used for the electrochemical cycling tests. The structural evolution during galvanostatic cycling of the different CAMs is depicted in **Figure 5**, where the evolution of the 002 diffraction peak of the initial P2 phase together with the corresponding voltage profiles between 1.5 and 4.6V are shown. The complete set of diffraction patterns collected during the operando experiments can be found in the supporting information in **Figures S9 and S10** (Supporting Information). The initial P2 structures are preserved for all investigated materials over a large voltage range during the second charge process. During this desodiation process the 002 reflections shift toward smaller angles, which is consistent with an increase of the *c* lattice parameters.^[10] When higher potentials are reached, the intensity of the 002 P2 reflection for NANMO, NANMFO, and NMFO decreases and broad, diffuse reflections occur at the high angle side of these reflections. This is due to the onset of a phase transformation to a so called “Z” phase or OP4 structure, which is an intermediate state between the transition of P2 into O2.^[10] A detailed overview of the evolution from the P2 structure to the “Z” phase at the high voltage region for the different materials is given in **Figure S10** (Supporting Information). In contrast, NAFMO shows no signs of such a phase transition in this experimental setup. To ensure that this unexpected behavior is a material effect, the measurement was repeated several times with different cells and cathode sheets.

In **Figure 6** the change of the lattice parameters of the P2 structures of the different CAMs during (de-)sodiation is shown. It needs to be noted that some small deviations from the lattice parameters calculated from the ex situ XRD data of the pristine materials are visible. This might be due to precycling with 1C (necessary for cyclable thick electrodes) and/or be of electrochemical nature, since cell assembly itself can introduce structural change as reported in literature.^[41] Lattice parameter *a* changes almost linearly for NAFMO, but for the other three materials where a phase transition occurs at high voltages, a broad minimum is visible. The lattice parameter *a* corresponds to the in-plane TM-TM-distance and the lattice parameter *c* corresponds to the layer to layer distance.^[10] During charging sodium ions are removed from between the layers. Lattice parameter *c* and the layer to layer distance increase due to the repulsive force between the layers, which were screened before by Na⁺. The increase of *c* stops shortly before the phase transition. Afterwards a drop of *c* in the high-voltage region can be seen. This drop shows different magnitudes depending on the cathode material. The drop in *c* arises probably from a similar effect like it is described for Li-based layered oxides in literature.^[42] The value of the *c* parameter is a combination of the heights of the Li-O and the TM-O slab. Kondrakov et al.^[42] explained the increase and drop of *c* during charging as follows: At the beginning the TM-O length is decreasing while the length of Li-O is increasing. In combination this leads to an increase in *c* because the magnitude of the Li-O change is larger. When the Li amount is low, both heights decrease at the same time, which becomes visible as a sudden drop in *c*. In case of NANMO and NANMFO a similar change in lattice parameters magnitude was observed. The different behavior of *c* at high volt-

age might be due to the oxidation of Fe³⁺ to Fe⁴⁺, which takes place at higher voltages than Ni³⁺/Ni⁴⁺ in P2 layered oxides.^[31,39] For NAFMO a moderate change of lattice parameter *a* together with the smallest change in *c* can be observed, which is related to the absence of a phase transition. If the charge-process was not complete for NAFMO, then this might be a reason for the absence. However, the measurement was repeated four times with different cathodes and electrode sheets. A phase transition was never visible. On top of that, we can refer to the Mößbauer spectroscopy. It revealed an oxidation of approximately 37% iron into the tetravalent state after charging. This amount was similar, but even higher than for NMFO with only 32%. This confirms that the NAFMO cathode material can be charged far enough for a possible high voltage phase transition, if there is any. A possible source of error in this experimental setup might also be the thickness of the cathode. In order to receive sufficient signal from the scattered x-rays the cathodes for the operando measurement were prepared with higher loading of active material (see Experimental Section). This resulted in approx. 80% of accessible capacity compared to thinner cathodes used for the electrochemical tests. However, all materials were treated in the same way and all showed this reduced capacity to similar extent. Therefore, it can be proclaimed that a possible phase transition for NAFMO might occur but is delayed much further into the high voltage region, while the other materials have already developed a transition. Recent work about layered sodium oxides has shown, that the introduction of many different elements into the crystal framework has improved cycling and structural stability, sometimes inhibiting the phase transition.^[43,44] Fu et al.^[18] demonstrated a synergetic effect when substituting with Ca and Mg at the same time. All this indicates that the design of the right chemical composition may cause less or a late phase transition, such as it is seemingly the case for NAFMO.

In case of NMFO the strongest change in both *a* and *c* was observed. This certainly has an influence on cycling stability (see later in electrochemistry) and demonstrates how aluminium doping (in case of NAFMO) improves the structure stability and hence the cycling behavior.^[17] A significant amount of lattice parameter change already occurred before the biphasic region, so even without the phase transition a difference between NMFO and NAFMO can be observed. In general, it can be seen, that the biphasic region is not centered at the point of maximum voltage. This might be due to several reasons like slow sodium ion kinetics,^[45] the thick electrode, or the current of C/10. A test with smaller current of e.g., C/20 and thinner cathodes might confirm that.

In P2-type layered oxides sodium ions can occupy two different prismatic sites within the structure, Na_e and Na_f, that share edges or faces. Neighboring sites cannot be occupied at the same time, which leads to vacancies and an ordering of these. The re-ordering of vacancies creates diffusional barriers with certain activation energies. Less ordering can be achieved with substitution elements such as Fe.^[16] In case of lithium, it is difficult to observe such occupancies due to the low electron density of Li and therefore less interaction with X-ray beam. Sodium is heavier, contains more electrons and hence more interaction with the X-ray beam leading to more reliable data about the occupancies. Therefore, we attempted a Rietveld refinement of the operando data including the sodium ion occupancies of the P2 structure within the

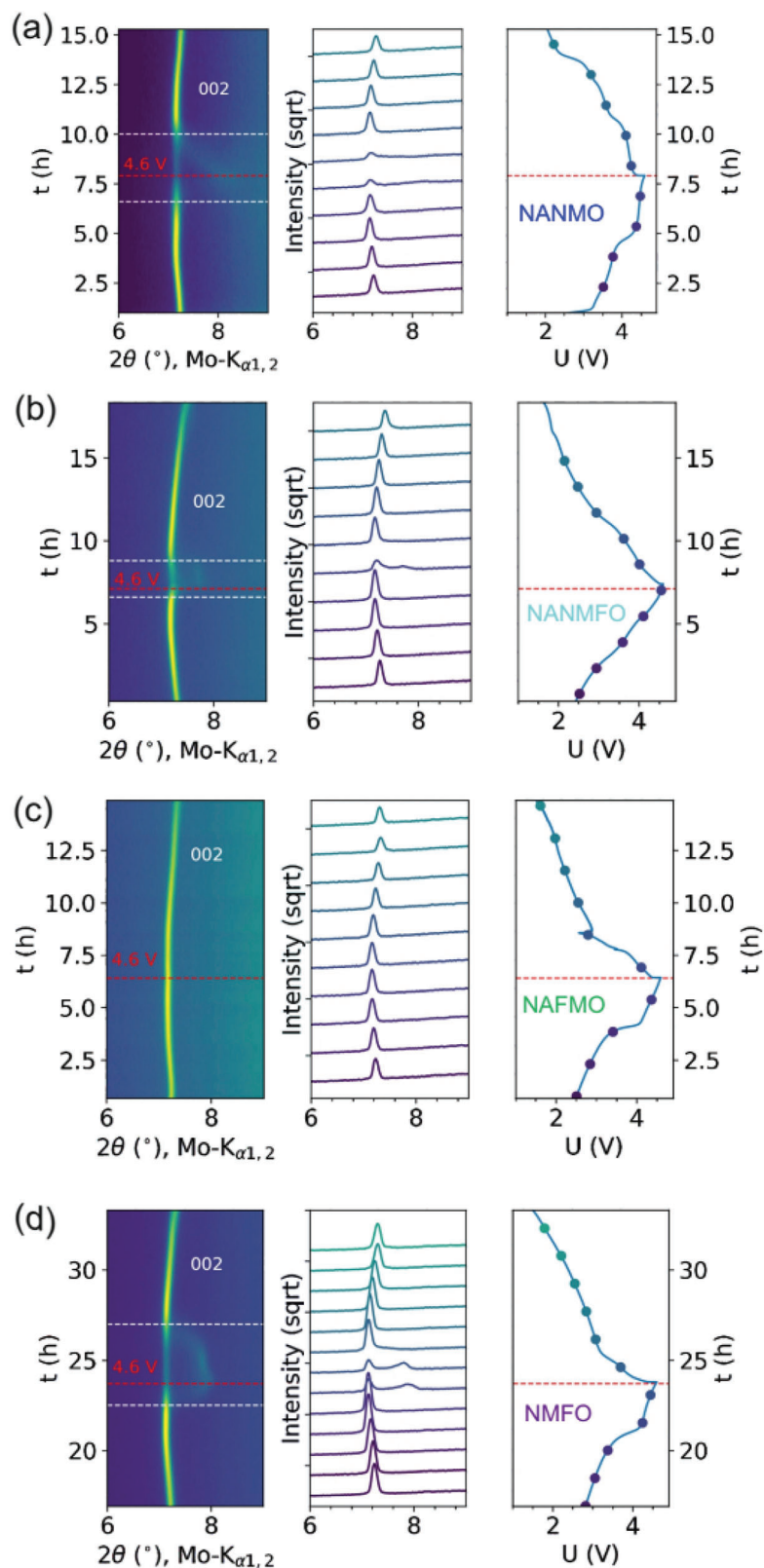


Figure 5. In situ XRD: Contour plot of the diffraction intensities measured during the 2nd cycle with C/10 of half-cells in the voltage window of 1.5 to 4.6V. The displayed 002 reflex is shifted during cycling due to change of lattice parameters. For all CAMs except NAFMO a phase transition is visible, most prominently seen with the intensity drop of the 002 reflex. The transition is not complete with the upper limit of 4.6V (marked with a red dashed line). The biphasic region is marked with dashed white lines. In case of NAFMO a leap in the discharge curve is visible at ca. 2.75V. This is most likely an artefact due to the reactive sodium metal anode.

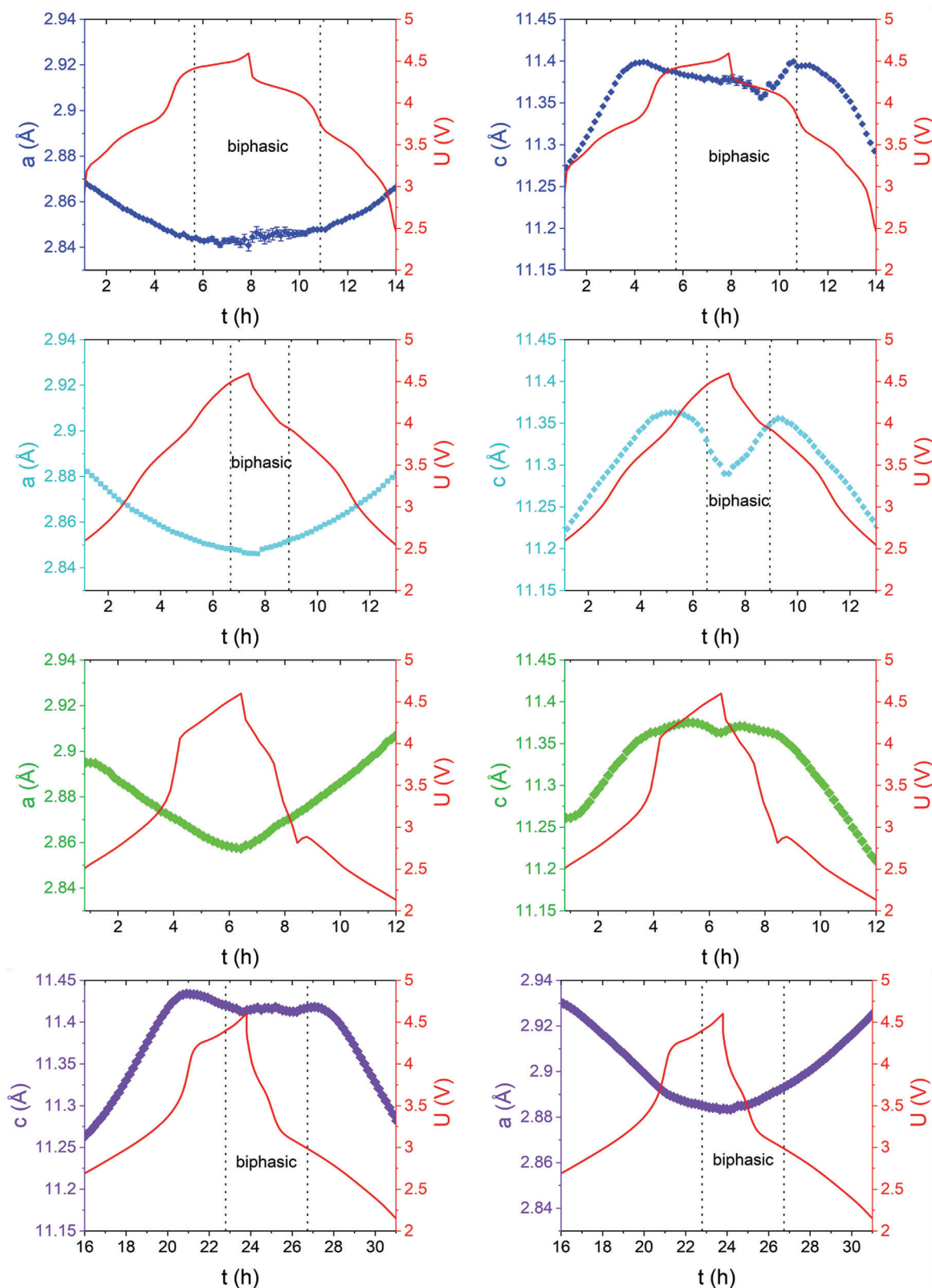


Figure 6. Refined parameters: The a -parameter is shown on the left-hand side and the c -parameter on the right-hand side, with the cell potential in red. During charging a contraction of the lattice along the a - and expansion along the c -axis can be seen (vice versa during discharging). Beyond 4.3V, the appearance of a new phase is marked as biphasic region. In case of NAFMO a leap in the discharge curve is visible at ca. 2.75V. This is most likely an artefact due to the reactive sodium metal anode.

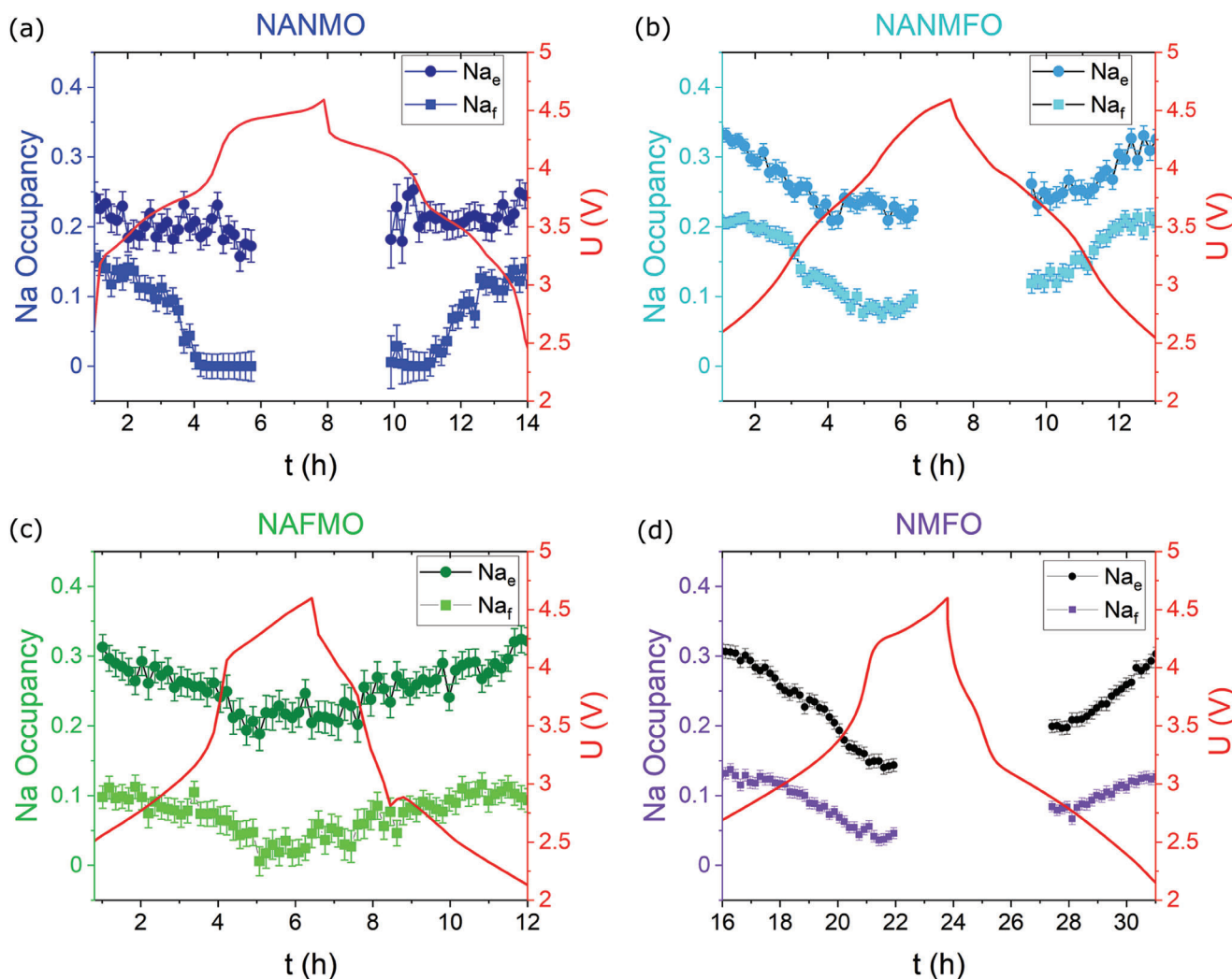


Figure 7. Sodium occupancy: Refined sodium ion occupancies for Na_e and Na_f within the P2-type structure. The chemical composition changes from high nickel to high iron content: NANMO (a), NANMFO (b), NAFMO (c) and NMFO (d). No unambiguous refinement was possible in the biphasic region. Sodium ions are removed from the layers during charging and both sodium sites get depleted (vice versa for discharging). In case of NAFMO a leap in the discharge curve is visible at ca. 2.75V. This is most likely an artefact due to the reactive sodium metal anode.

one-phase region. It should be noted here, that the refined occupation values may deviate from the actual, absolute values due to the limited quality of the operando XRD data, but the qualitative trends should be meaningful. The refined occupancies are presented in Figure 7. All materials exhibit higher occupancies for the Na_e sites compared to the Na_f sites. However, the refined values for both sodium sites are lower compared to the ex situ XRD refinements. The reason for that is likely to be the same as before in case of the lattice parameters (structural change introduced due to cell assembly^[41] and pre-cycling with 1C).

For NANMO the occupancy of Na_e is slightly decreasing while that of Na_f is decreasing much faster with a drop to zero. The same behavior was observed vice versa for discharging, when the sodium sites are refilled. This tells us that the depletion and filling of Na_f is favored over Na_e . In case of NANMFO and NAFMO a similar trend for both sites in filling and depletion is visible, so neither of the two sites appears to be favored over the other during charge and discharge. For NMFO a steeper slope for Na_e

than for Na_f is visible. In this case Na_e is favored over Na_f during charge and discharge (vice versa to NANMO), but less distinctive as for NANMO. This effect can best be understood when comparing NANMO and NANMFO: Less vacancy ordering can be achieved when a substitutional element is introduced into the crystal framework.^[16] Less vacancy ordering (Figure 7b) leads to lower activation energy barriers for the ionic hopping process. This lower ionic activation energy E_{A_i} was also found with impedance spectroscopy, when comparing the Arrhenius plots of NANMO and NANMFO shown above (Figure 4). With this property there is no preferred sodium site for depletion and re-filling, which results in the absence of distinctive voltage plateaus in case of NANMFO.^[16] In total, the reduced vacancy ordering is the reason for enhanced Na^+ diffusion, seen as a smaller slope in the Arrhenius plot (Figure 4), which does not necessarily imply a higher conductivity. When comparing the electrochemical performance of half-cells with NANMO and NANMFO it can be seen, that the reduced vacancy ordering of NANMFO improves

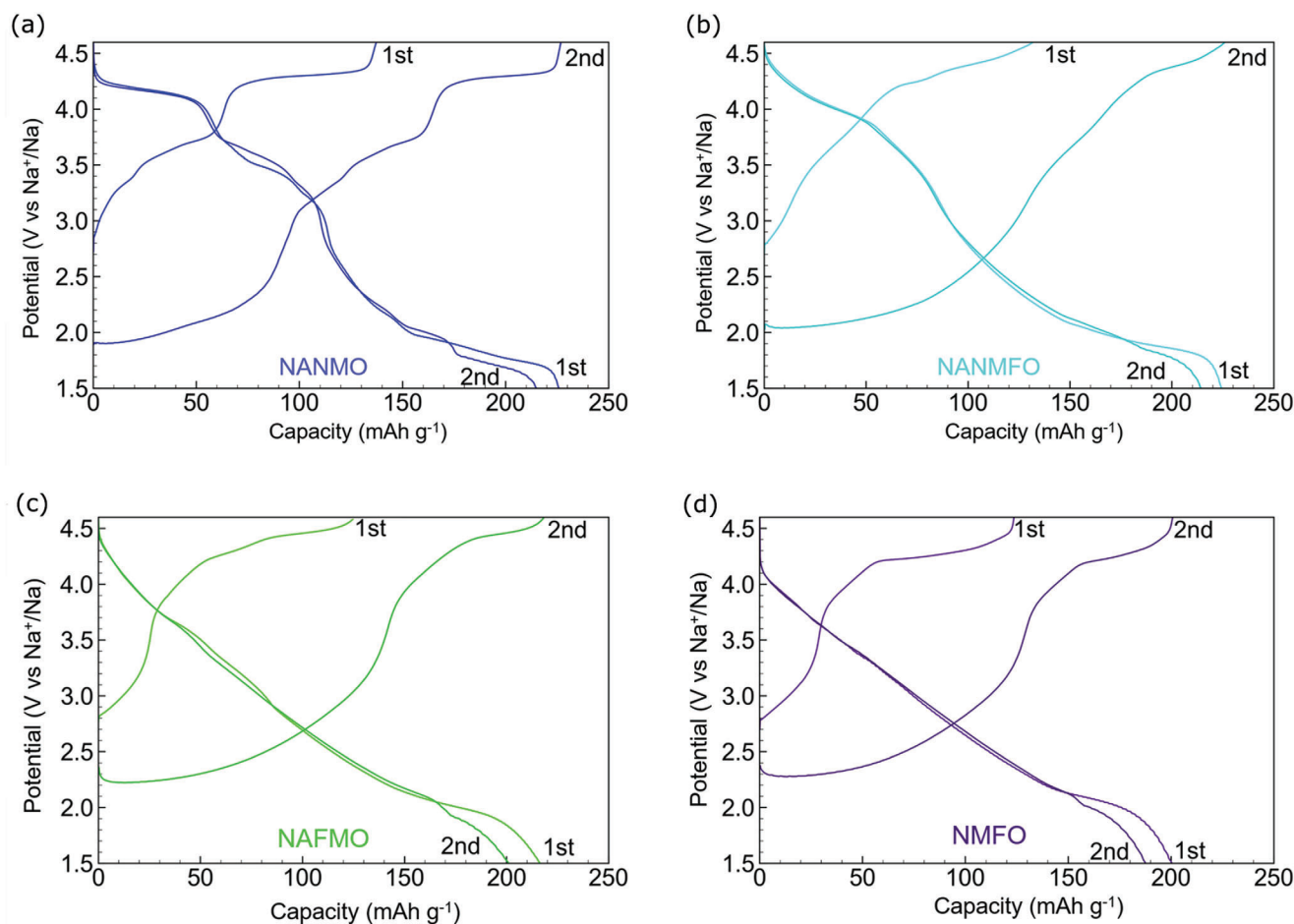


Figure 8. Charge-Discharge-Curves: Displayed are first cycle with C/20 and the second cycle with C/10 of the four different CAMs. The plots show the capacity gain in the 2nd cycle from the sodium anode. The different materials in (a–d) exhibit altered shape of redox plateaus.

the rate-capability for moderate and high C-rates (see Figure 9). A comparison of the electrochemistry of these two CAMs is particularly possible since both active materials exhibit quite similar morphologies (porosity and specific surface area). In case of NAFMO there is also a less distinctive voltage plateau visible and no preferred sodium site. NMFO exhibits similar less distinctive voltage plateaus but here a slight preference of Na_c was observed. In conclusion it can be said that the sodium vacancy ordering depends strongly on the chosen chemical composition and was reduced in this investigation when iron is present.

2.6. Electrochemical Performance

Different open circuit voltages (OCV) were observed for the different cathode materials in half-cells: 2.75, 2.69, 2.70, and 2.69V for NANMO, NANMFO, NAFMO, and NMFO, respectively. In Figure 8 the charge–discharge-curves of the first two cycles of a rate-test with half-cells are shown (Figure S12, Supporting Information) displays the curves of the other rates in the following rate-test). For NANMO clear voltage plateaus are visible (a). When half of the nickel content is substituted with iron to NANMFO the plateaus are less pronounced (b). This corresponds to the reduced

sodium vacancy ordering as described before in the section about operando XRD. In case of NAFMO (c) and NMFO (d) plateaus are visible, but are less distinctive than for NANMO. In the first charge cycle the received capacity corresponds to the sodium amount in the structure (measured with ICP-OES, see Supporting Information). A contribution of sodium is possible due to the oxidation of the transition metals in the layered oxide. It can be calculated that at least for NANMO and NANMFO also oxygen oxidation $\text{O}^{2-}/(\text{O}_2)^{0}$ must have been involved to achieve the specific capacity in the first charge cycle. This indicates that during the electrochemical test a phase transition involving oxygen oxidation, takes place, as it was found before with operando XRD. Therefore electrochemical cycling was performed with three different upper voltage limits 4.6, 4.3, and 4.0V in order to step-wise reduce cycling in this critical high voltage region. The influence on capacity, rate-capability and cycling-stability will be individually discussed in the following. In Figure 8 it can be seen that in the second cycle the specific capacity exceeds the theoretical one, due to additional sodium from the Na metal anode. P2-type structures are sodium deficient: $\text{Na}_{0.6}\text{TMO}_2$ (TM = transition metal). Only 0.6 sodium equivalent per formula are available. Cycling below the OCV in half-cells adds more sodium. This effect increases capacity, but is not accessible in full cells without pre-sodiation.

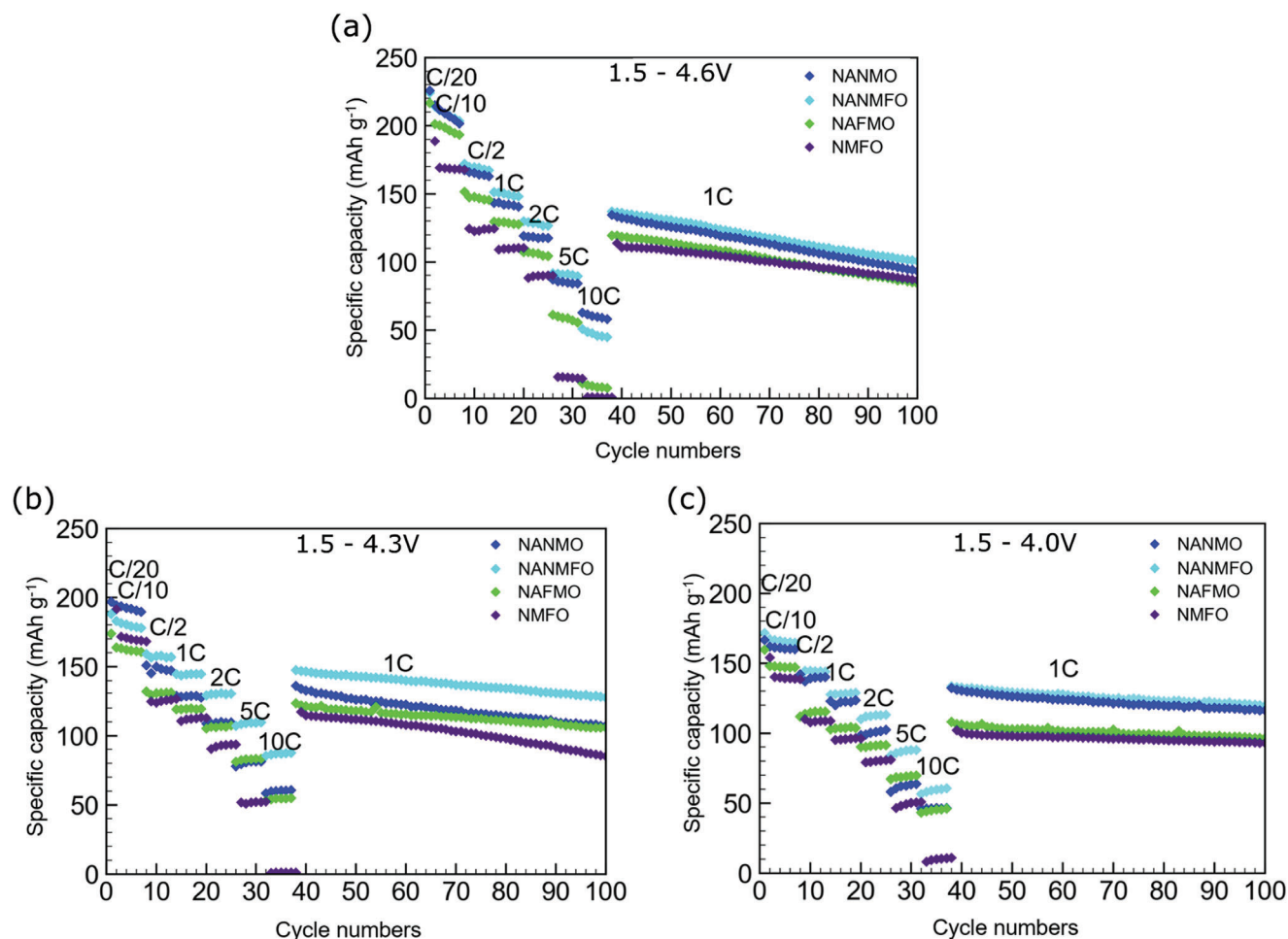


Figure 9. Half-cell cycling: All four CAMs sintered at $T_S = 950^\circ\text{C}$. Cycling vs. Na-anode with different upper limits: a) 4.6V, b) 4.3V, and c) 4.0V. Rate-test at the beginning and long term cycling with 1C. The corresponding charge–discharge-curves are displayed in Figure 8 and Figure S12–S14 (Supporting Information).

The average voltage (AV) during discharge is decreasing with the iron content. The measured average voltages between 1.5 and 4.6V in the discharge cycle with a C/20 rate are $AV_{\text{NANMO}} = 2.96\text{V}$, $AV_{\text{NANMFO}} = 2.88\text{V}$, $AV_{\text{NAFMO}} = 2.80\text{V}$ and $AV_{\text{NMFO}} = 2.7\text{V}$. This decrease in the average voltage originates from the different voltage profiles shown in Figure 8. For NANMO distinctive voltage plateaus at high voltages are visible, resulting in a higher average voltage. In case of NANMFO these high voltage plateaus are smoothed out and therefore a smaller AV is measured. Increasing the iron amount further (NAFMO and NMFO) leads to an almost linear slope of the discharge-curve and shifts them into the low voltage area. In such cases, a discharge plateau is not visible at high voltage, only one at approx. 2.0V.

2.6.1. Rate-Capability

A rate test followed by a long-term cycling test are shown in Figure 9. The cells were cycled with different upper cut-off limits: a) 4.6V, b) 4.3V, and c) 4.0V. Lower limit was always 1.5V. In general nickel containing materials (NANMO and NANMFO) exhibit

higher initial specific capacities. With 4.6V as upper limit (UL) NANMO and NANMFO are almost identical in performance. In case of 4.3V as upper limit the best performance was observed for NANMFO. With 4.0V as upper limit NANMO and NANMFO perform again almost identical. Nickel containing materials show in general higher capacity. An overview of the rate-capability is given in Figure S11 (Supporting Information), where the relative discharge capacity as a function of the C-rate is shown. The charge–discharge curves during the rate-test are displayed in Figures S12, S13, and S14 (Supporting Information). It can be seen that for the iron containing materials an increase of iron leads to a decrease in the rate-capability. This correlates with the increasing primary particle size due to increased sinter activity and corresponding longer diffusion paths within the particles (see Figure 2; Table S2, Supporting Information). The size of primary particles has a strong influence on the rate-capability. Especially in combination with the diffusivity in the active material the influence of the primary particle size differs. While for materials with a high diffusivity the size of the primary particles has no influence on the rate capability, for low diffusion constants, the particle size plays an important role for the rate-capability.^[46]

In general the rate performance of NANMFO and NAFMO is quite similar due to small differences in the micro structure, whereas the large particles sizes of NMFO result the worst rate-capability.

The course of the C-rate dependence differs significantly for NANMO from that of the Fe-containing materials. While at low C-rates the drop in Figure S11 (Supporting Information) is still relatively strong and comparable to NMFO, the drop is smaller at high C-rates. The reason for this is, on the one hand, the small primary particle size and, on the other hand, the one order of magnitude higher electronic conductivity as determined by EIS. Naumann et al.^[46] have demonstrated how electronic conductivity in the material influences the rate capability as a function of porosity and secondary particle size. At good electronic conductivities, the particle morphology is not limiting, only at lower conductivities do the differences in microstructure or secondary particle morphology become noticeable. Thus, with the same microstructure/porosity or secondary particle size but different electronic conductivities, the rate capability can vary greatly. This is evident here when comparing NANMO and NANMFO, which have comparable particle properties but different electronic conductivities, and the better conductivity of NANMO results in better relative C-rate capability.

Related to the ionic part of conductivity is the aspect of sodium vacancy ordering as described before, which should also be mentioned in this discussion. NANMFO is slightly more stable at moderate and high C-rates during rate-test (exception at 10C and with UL = 4.6V). With 4.3V (Figure 9b) as upper limit NANMFO delivers more capacity for moderate and high C-rates as compared to NANMO. This is related to less vacancy ordering in case of NANMFO (see operando XRD data in Figure 7). Less ordering lowers diffusion barriers for sodium transport which is best seen at moderate and high C-rates.^[16] Before, with the upper limit 4.6V, this was only slightly visible, since the strong degradation for all materials is obscuring the effect. It is also worth mentioning that for NANMFO the phase transition starts at a higher cell voltage (as seen in Figure 5).

With UL = 4.0V NANMO and NANMFO are almost identical, just for moderate to high rates slightly better performance of NANMFO is observed, most probably due to the same vacancy ordering effect.

For NAFMO a similar effect of less vacancy ordering was observed with in operando XRD and is visible in the windows 1.5 to 4.3V and 1.5 to 4.0V, although it is less distinct. At small rates NANMO exhibits higher specific capacity (due to its advantageous particle morphology), but with moderate rates (1C – 5C) the difference between NANMO and NAFMO becomes smaller, due to the absence of vacancy ordering in NAFMO.

2.6.2. Cycling Stability

Table 3 summarizes the electrochemical performance in terms of discharge capacities in some specific cycles for all cathode materials and for the three cycling windows. An upper cut-off limit of 4.6V (Figure 9a) results in a strong degradation, which can be ascribed to the occurrence of phase transitions in the high voltage region beyond 4.0V.^[23] Operando XRD (see Figure 5) has re-

Table 3. Summary of electrochemical performance: Data taken from Figure 9. Specific capacities from cycle 1, 39, and 100. The capacity retention obtained with different upper voltage limits can be compared in the last row. The retention refers to the last 61 cycles with 1C.

	1,5 – 4.6 V			
	NANMO	NANMFO	NAFMO	NMFO
Discharge capacity				
1. Cycle (C/20)	225	226	217	190
39. Cycle (1C)	135	137	120	110
100. Cycle (1C)	93	101	85	79
Retention	68,9%	73,7%	70,8%	71,8%
	1,5 – 4.3 V			
	NANMO	NANMFO	NAFMO	NMFO
Discharge capacity				
1. Cycle (C/20)	196	189	171	191
39. Cycle (1C)	138	148	121	117
100. Cycle (1C)	108	128	102	84
Retention	78,3%	86,5%	84,3%	71,8%
	1,5 – 4.0 V			
	NANMO	NANMFO	NAFMO	NMFO
Discharge capacity				
1. Cycle (C/20)	166	172	160	154
39. Cycle (1C)	135	134	108	102
100. Cycle (1C)	119	120	94	93
Retention	88,1%	89,6%	87,0%	91,2%

vealed that all CAMs but NAFMO exhibit a phase transition in this region. Even without an observed phase transition NAFMO shows degradation. One reason for that is severe change in the lattice parameters *a* and *c* (see Figure 6). Another reason might be, that in case of NAFMO a phase transition might be delayed to higher voltages or higher sodium amounts to be extracted. The latter could occur with thinner cathodes, such as used for the electrochemical cycling presented in this section (see Experimental Section). Reducing or avoiding the phase transition and lattice stress by lowering the upper limit to 4.3 and 4.0V (Figure 9b,c) improves long term stability. With Table 3 it can be seen, that the retention is similar for the individual materials in windows 1.5 to 4.6V and 1.5 to 4.0V, with 71% and 89% average retention. However, it can be noted that in cycle 39. (begin of long-term cycling with 1C) the nickel containing materials exhibit higher capacities than the others.

In the window 1.5 to 4.3V NANMFO and NAFMO exhibit a better stability than NANMO and NMFO. There are several possible reasons for this behavior. From Figure S5.12 (Supporting Information) it is evident that polarization of the cells is increasing for all materials, especially for NMFO. Another reason for the different long-term stability of the four materials might be that the biphasic region for NANMFO starts at higher voltage than for NANMO (see in situ XRD in Figure 5). Therefore, when an upper limit of 4.6V is used in the cycling tests, both materials

exhibit a phase transformation to a Z-phase, which results in a similar degradation behavior. Lowering the cut-off value to 4.3V prevents this phase transition for NANMFO, whereas NANMO still undergoes this transition. This reduces the material degradation for NANMFO, while at the same time relative high capacities are maintained.

Further reducing the cut-off voltage down to 4.0V leads to an improved stability for all materials due to avoidance of severe structural changes and phase transitions. In the voltage window 1.5 to 4.0V the iron containing materials (NAFMO, NMFO) show better long-term cycling stability than nickel containing materials (NANMO, NANMFO). The reason for that is unclear. The long-term stability of NAFMO and NMFO is almost identical, which means that aluminium substitution for NAFMO has no effect on cycling-stability when cycled only up to 4.0V. The beneficial role of aluminium becomes apparent at higher voltages but there is a trade off against the lower specific capacity.

3. Conclusion

In summary, we presented a two-step spray-drying synthesis process, which can be easily adapted for the production of larger amounts of cathode active materials for SIBs. We synthesised four different P2-type cathode materials consisting of hierarchically structured particles. The nickel contains layered oxide $\text{Na}_{0.6}\text{Al}_{0.11}\text{Ni}_{0.22}\text{Mn}_{0.66}\text{O}_2$ (NANMO) serves as a reference material. The gradual substitution of nickel with environmental benign and cost-effective iron yielded the other investigated materials: $\text{Na}_{0.6}\text{Al}_{0.11}\text{Ni}_{0.11}\text{Mn}_{0.66}\text{Fe}_{0.11}\text{O}_2$ (NANMFO), $\text{Na}_{0.6}\text{Al}_{0.11}\text{Fe}_{0.22}\text{Mn}_{0.66}\text{O}_2$ (NAFMO) and $\text{Na}_{0.6}\text{Mn}_{2/3}\text{Fe}_{1/3}\text{O}_2$ (NMFO). The micro structure of the hierarchically structured particles, particularly porosities and specific surface area, depend strongly on chemical composition. When substituting Ni with Fe, the porosity and surface area decrease. This effect is caused by the higher sinter activity when the iron content is increased, which also results in an increased grain growth. NMFO shows the largest grain sizes and the lowest internal porosity within the granules. Therefore, this material exhibits a low rate-capability and the lowest specific capacity. Partial substitution of iron with aluminium (NAFMO) seems to suppress the phase transition on deep charge at high voltages, which demonstrates the beneficial role of aluminium doping for the structural stability of Na-battery cathodes. Of these four layered oxide materials, the most promising is NANMFO, which has a high initial capacity and good capacity retention in each voltage window. The properties in the voltage window from 1.5 to 4.3V are noteworthy: NANMFO shows a very good initial capacity of 189mA h g^{-1} at C/20 and 148mA h g^{-1} even at 1C. The capacity retention after 100 cycles exceeds that of the other materials with 86.5%. Even at 10C this material shows a capacity retention of 50%. The potential of this material class can only be exploited, if the structural prerequisites for good electrochemical performance are met by the chemical composition. This is made possible by suitable synthesis conditions and thus an ideal micro structure. The material design must be adapted to the intended utilisation profile of such sodium-ion-battery cells, whereby limits are set with regard to the usable voltage window.

4. Experimental Section

Synthesis: The following reactants were used for the precursor preparation: Sodium acetate anhydrous (99% Merck), Aluminium nitrate nonahydrate (98% Organics), Nickel(II) acetate tetrahydrate (99% Aldrich Chemistry), Iron(III) nitrate nonahydrate (98% Alfa Aesar), Manganese(II) acetate tetrahydrate (99% Aldrich Chemistry). The chemicals were dissolved in the right ratio for the different materials in different containers in deionized water and were stirred overnight. The solutions were combined and stirred for another hour, followed by spray drying (Mobile Minor, GEA) with an inlet temperature of 200°C and an outlet temperature of 108°C (batch size approx. 200 to 600g). The obtained precursor powders underwent a two-step heat treatment. First at 1000°C in air to remove the organics of the reactants. Grinding in a Pulverisette five planetary mill (Fritsch) with 3mm ZrO_2 milling balls in deionized water for 24h (planetary disk at 206rpm, bowl at 447rpm) resulted in an aqueous suspension of fine primary particles. This suspension was spray dried again with the same parameters as before into a fine powder of secondary particles (batch size approx. 50 to 100g). The spray dried powders were finally calcined at 950°C in air with a dwell time of 6h and heating rate of 5°C min^{-1} .

Material Characterization: A Supra 55 (Zeiss) scanning electron microscope (SEM) was used to visualize the morphology of the spray dried particles. The specific surface area was investigated with a Gemini VII 2390a (NSA, Micromeritics) and calculated with the Brunauer-Emmet-Teller (BET) method. Porosity of the secondary particles was measured with mercury intrusion with a CEI Pascal 1.05 (Thermo Electron). To control the chemical composition of the cathode materials, inductively coupled plasma optical emission spectroscopy (ICP-OES) was performed (iCAP 7600 Duo, Thermo Fisher Scientific). The carbon content was measured with a CS-analyser and oxygen with carrier gas hot extraction (TGHE). The particle size distribution was measured via laser diffraction (Horiba LA950, Retsch Technology). Mößbauer spectroscopy was used to investigate the $\text{Fe}^{3+}/\text{Fe}^{4+}$ ratio of the iron containing samples in their pristine state and after being fully charged. ^{57}Fe Mößbauer spectroscopy was performed at room temperature on a WissEL constant-acceleration spectrometer in transmission mode with a ^{57}Co (Rh) source. X-ray diffraction (XRD) was performed ex situ on a D8-Advance (Bruker) with $\text{Cu K}_{\alpha 1,2}$ radiation (mean wavelength $\lambda = 1.54184\text{\AA}$) and a Lynxeye XE-T detector.

Electrochemical Experiments: Electrode preparation was done by mixing the cathode powder with an N-Methyl-2-pyrrolidone (NMP) based slurry with polyvinylidene fluoride (PVDF, Sigma-Aldrich) and the conductive carbon TIMCAL-C65 in a mass ratio of 80:10:10 in a SpeedMixer DAC 150 (Hauschild). The mixture was coated on aluminium foil with the doctor blade method, a gap size of $200\mu\text{m}$ and a speed of 1.5m s^{-1} on the device Coatmaster 510 (Erichsen) and dried with 120°C under vacuum overnight. Average active material mass loading of prepared cathode sheets was 3.3mg cm^{-2} . Cathodes with a diameter of 12mm were punched and pressed with a force of 5kN. Half cells were built as coin cells CR2032 with the cathodes, 16mm diameter glass fibre separator (Whatman GF/C, $260\mu\text{m}$ thickness), a 12mm sodium metal anode. As electrolyte were used $100\mu\text{L}$ of Propylene Carbonate (PC) with 1M NaPF_6 and 5% Fluoroethylene (FEC). Galvanostatic cycling with potential limitation was performed on an Arbin potentiostat in the electrochemical window of 1.5 to 4.0 / 4.3 / 4.6 V versus Na^+/Na . The current of 1C for cycling was defined according to Hasa et al.^[23] based on the theoretical capacity with 0.6 Na of the pristine structure, which resulted in the currents of $I_{\text{NANMO}} = 164\text{mA g}^{-1}$, $I_{\text{NANMFO}} = 165\text{mA g}^{-1}$, $I_{\text{NAFMO}} = 165\text{mA g}^{-1}$ and $I_{\text{NMFO}} = 159\text{mA g}^{-1}$. To make sure the discharge step starts with a fully desodiated cathode the charge current was kept at small values during the rate-test. For small discharge rates, such as C/20 and C/10 the same rate was used for charging and for discharge rates beyond C/2 the current for charging was kept at C/2. At the beginning of a electrochemical cycling formation cycle with 1C was performed (not shown).

Electrochemical Experiments—Impedance: Electrochemical impedance spectroscopy (EIS) was performed on pure cathode material without any binder or conductive carbon. The powders received after the second spray drying process (before second heat treatment) were

pressed with a PW10 manual laboratory press with a force of 20kN and a press tool with a diameter of 12mm into pellets. The resulting thickness depends on the used powder and varies between 0.9 and 1.2mm. The pellets were sintered at 950°C for 6h. Afterward they were dry smoothed with sand paper (grit size 1000) and sputtered with gold on both sides. To improve the connection in silver ink was added to both sides on top. Vacuum drying at 120°C was done to remove any moisture and the pellets were finally assembled into Swagelok cells under an argon atmosphere. For the EIS measurements a VSP-300 (BioLogic) potentiostat was used with 50mV amplitude in the range from 7MHz to 10mHz. The cells were kept in a BTZ-175 (ESPECS) climate chamber. Temperature was set in 5 °C steps between to 60 °C. Before measurement the system waited 0.5h to 1h until the temperature chamber was stable and another waiting period of 1h was implemented to make sure, the Swagelok cells had adopted the temperature.

Electrochemical Experiments—Operando X-Ray Diffraction: For operando XRD measurements a laboratory diffractometer for battery research with Mo- $K_{\alpha 1/2}$ radiation was used.^[47] To increase the intensity thicker cathodes were prepared as described above but with a gap size at the doctor blade of 400 μ m, which resulted in a mass loading of 8.0 to 9.5mg cm⁻². Coin cells with polyimide windows were prepared and after a formation cycle the current during XRD measurement was C/10. Acquisition time for each diffraction pattern was 10 min which corresponds to $\Delta x \approx 0.01$ in Na_xTMO₂. Rietveld refinement was executed with the software Topas V6.

Supporting Information

Supporting Information is available from the Wiley Online Library or from the author.

Acknowledgements

The authors thankfully acknowledged the support of Dr. Thomas Bergfeldt (Institute of Applied Materials - Applied Material Physics, KIT) for the chemical analysis of the composition with ICP-OES and other methods. This work was completed as part of the CELEST (Center for Electrochemical Energy Storage Ulm-Karlsruhe). Funding was made possible by the German Research Foundation (DFG) under the Cluster of Excellence PO-LiS (Post Lithium Storage).

Open access funding enabled and organized by Projekt DEAL.

Conflict of Interest

The authors declare no conflict of interest.

Data Availability Statement

The data that support the findings of this study are openly available in zenodo at <http://doi.org/10.5281/zenodo.10118614>.

Keywords

hierarchical structure, sodium-ion-battery, spray drying

Received: June 14, 2023
Revised: October 24, 2023
Published online:

[1] S. B. Wali, M. Hannan, M. Reza, P. J. Ker, R. Begum, M. Abd Rahman, M. Mansor, *J. Energy Storage* **2021**, *35*, 102296.

- [2] M. Baumann, M. Häringer, M. Schmidt, L. Schneider, J. F. Peters, W. Bauer, J. R. Binder, M. Weil, *Adv. Energy Mater.* **2022**, *12*, 2202636.
- [3] C. Vaalma, D. Buchholz, M. Weil, S. Passerini, *Nat. Rev. Mater.* **2018**, *3*, 1.
- [4] G. Haxel, *Rare earth elements: critical resources for high technology*, vol. 87, US Department of the Interior, US Geological Survey, Reston, VA **2002**.
- [5] R. C. Massé, E. Uchaker, G. Cao, *Sci. China Mater.* **2015**, *58*, 715.
- [6] T. Koketsu, J. Ma, B. J. Morgan, M. Body, C. Legein, W. Dachraoui, M. Giannini, A. Demortiere, M. Salanne, F. Dardoize, H. Groult, O. J. Borkiewicz, K. W. Chapman, P. Strasser, D. Dambournet, *Nat. Mater.* **2017**, *16*, 1142.
- [7] G. A. Elia, K. Marquardt, K. Hoepfner, S. Fantini, R. Lin, E. Knipping, W. Peters, J.-F. Drillet, S. Passerini, R. Hahn, *Adv. Mater.* **2016**, *28*, 7564.
- [8] A. Rudola, A. J. Rennie, R. Heap, S. S. Meysami, A. Lowbridge, F. Mazzali, R. Sayers, C. J. Wright, J. Barker, *J. Mater. Chem. A* **2021**, *9*, 8279.
- [9] P. Yan, J. Zheng, M. Gu, J. Xiao, J.-G. Zhang, C.-M. Wang, *Nat. Commun.* **2017**, *8*, 1.
- [10] J. W. Somerville, A. Sobkowiak, N. Tapia-Ruiz, J. Billaud, J. G. Lozano, R. A. House, L. C. Gallington, T. Ericsson, L. Häggström, M. R. Roberts, U. Maitra, P. G. Bruce, *Energy Environ. Sci.* **2019**, *12*, 2223.
- [11] N. Voronina, M.-Y. Shin, H.-J. Kim, N. Yaqoob, O. Guillon, S. H. Song, H. Kim, H.-D. Lim, H.-G. Jung, Y. Kim, H.-K. Lee, K.-S. Lee, K. Yazawa, K. Gotoh, P. Kaghazchi, S.-T. Myung, *Adv. Energy Mater.* **2022**, *12*, 2103939.
- [12] R.-M. Gao, Z.-J. Zheng, P.-F. Wang, C.-Y. Wang, H. Ye, F.-F. Cao, *Energy Storage Mater.* **2020**, *30*, 9.
- [13] M. Chen, Q. Liu, S.-W. Wang, E. Wang, X. Guo, S.-L. Chou, *Adv. Energy Mater.* **2019**, *9*, 1803609.
- [14] Y. Lei, X. Li, L. Liu, G. Ceder, *Chem. Mater.* **2014**, *26*, 5288.
- [15] D. Dewar, A. M. Glushenkov, *Energy Environ. Sci.* **2021**, *14*, 1380.
- [16] N. Wang, H.-R. Yao, X.-Y. Liu, Y.-X. Yin, J.-N. Zhang, Y. Wen, X. Yu, L. Gu, Y.-G. Guo, *Sci. Adv.* **2018**, *4*, eaar6018.
- [17] S. Kim, K. Min, K. Park, *J. Alloys Compd.* **2021**, *874*, 160027.
- [18] H. Fu, Y.-P. Wang, G. Fan, S. Guo, X. Xie, X. Cao, B. Lu, M. Long, J. Zhou, S. Liang, *Chem. Sci.* **2022**, *13*, 726.
- [19] A. C. Wagner, N. Bohn, H. Geßwein, M. Neumann, M. Osenberg, A. Hilger, I. Manke, V. Schmidt, J. R. Binder, *ACS Appl. Energy Mater.* **2020**, *3*, 12565.
- [20] W. Ren, M. Qin, Y. Zhou, H. Zhou, J. Zhu, J. Pan, J. Zhou, X. Cao, S. Liang, *Energy Storage Mater.* **2023**, *54*, 776.
- [21] P. Vass, E. Szabó, A. Domokos, E. Hirsch, D. Galata, B. Farkas, B. Démuth, S. K. Andersen, T. Vigh, G. Verreck, G. Marosi, Z. K. Nagy, *Wiley Interdiscip. Rev.: Nanomed. Nanobiotechnol.* **2020**, *12*, e1611.
- [22] B. Vertruyen, N. Eshraghi, C. Piffet, J. Bodart, A. Mahmoud, F. Boschini, *Materials* **2018**, *11*, 1076.
- [23] I. Hasa, S. Passerini, J. Hassoun, *J. Mater. Chem. A* **2017**, *5*, 4467.
- [24] K. K. Das, R. C. Reddy, I. B. Bagoji, S. Das, S. Bagali, L. Mullur, J. P. Khodnapur, M. Biradar, *J. Basic Clin. Physiol. Pharmacol.* **2018**, *30*, 141.
- [25] N. Yabuuchi, M. Kajiyama, J. Iwatate, H. Nishikawa, S. Hitomi, R. Okuyama, R. Usui, Y. Yamada, S. Komaba, *Nat. Mater.* **2012**, *11*, 512.
- [26] E. Talaie, V. Duffort, H. L. Smith, B. Fultz, L. F. Nazar, *Energy Environ. Sci.* **2015**, *8*, 2512.
- [27] P. W. Stephens, *J. Appl. Crystallogr.* **1999**, *32*, 281.
- [28] B. U. Köhler, M. Jansen, *Z. Anorg. Allg. Chem.* **1986**, *543*, 73.
- [29] M. A. Denecke, W. Gunsser, G. Buxbaum, P. Kuske, *Mater. Res. Bull.* **1992**, *27*, 507.
- [30] Y. Nanba, T. Iwao, B. M. d. Boisse, W. Zhao, E. Hosono, D. Asakura, H. Niwa, H. Kiuchi, J. Miyawaki, Y. Harada, M. Okubo, A. Yamada, *Chem. Mater.* **2016**, *28*, 1058.

- [31] N. P. Phuong Le, N. L. T. Huynh, A. Le Bao Phan, D. T. Ngoc Nguyen, T. T. Thu Nguyen, H. V. Nguyen, X. Cui, A. Garg, P. M. L. Le, M. V. Tran, *J. Chem.* **2021**, 2021, 1.
- [32] J. Zahnw, T. Bernges, A. Wagner, N. Bohn, J. R. Binder, W. G. Zeier, M. T. Elm, J. Janek, *ACS Appl. Energy Mater.* **2021**, 4, 1335.
- [33] C. Julien, A. Mauger, A. Vijn, K. Zaghbi, C. Julien, A. Mauger, A. Vijn, K. Zaghbi, *Lithium Batteries*, Springer, Berlin, Heidelberg **2016**.
- [34] K. Walczak, K. Redel, R. Idczak, R. Konieczny, K. Idczak, V. H. Tran, A. Plewa, M. Zikabka, M. Rybski, J. Tobola, J. Molenda, *Energy Technol.* **2022**, 10, 2101105.
- [35] Z. Wang, W. Yang, J. Yang, L. Zheng, K. Sun, D. Chen, L. Sun, X. Liu, *Ceram. Int.* **2020**, 46, 12965.
- [36] H. V. Ramasamy, K. Kaliyappan, R. Thangavel, W. M. Seong, K. Kang, Z. Chen, Y.-S. Lee, *J. Phys. Chem. Lett.* **2017**, 8, 5021.
- [37] R. Christensen, G. Olson, S. W. Martin, *J. Phys. Chem. B* **2013**, 117, 16577.
- [38] R. Amin, Y.-M. Chiang, *J. Electrochem. Soc.* **2016**, 163, A1512.
- [39] Y. Xiao, Y.-F. Zhu, H.-R. Yao, P.-F. Wang, X.-D. Zhang, H. Li, X. Yang, L. Gu, Y.-C. Li, T. Wang, Y.-X. Yin, X.-D. Guo, B.-H. Zhong, Y.-G. Guo, *Adv. Energy Mater.* **2019**, 9, 1803978.
- [40] D. Carlier, M. Ménétrier, C. Delmas, *J. Mater. Chem.* **2001**, 11, 594.
- [41] D. Mohanty, S. Kalnaus, R. A. Meisner, K. J. Rhodes, J. Li, E. A. Payzant, D. L. Wood III, C. Daniel, *J. Power Sources* **2013**, 229, 239.
- [42] A. O. Kondrakov, H. Geßwein, K. Galdina, L. De Biasi, V. Meded, E. O. Filatova, G. Schumacher, W. Wenzel, P. Hartmann, T. Brezesinski, J. Janek, *J. Phys. Chem. C* **2017**, 121, 24381.
- [43] Y. Wang, L. Wang, H. Zhu, J. Chu, Y. Fang, L. Wu, L. Huang, Y. Ren, C.-J. Sun, Q. Liu, X. Ai, H. Yang, Y. Cao, *Adv. Funct. Mater.* **2020**, 30, 1910327.
- [44] P.-F. Wang, Y. You, Y.-X. Yin, Y.-G. Guo, *Adv. Energy Mater.* **2018**, 8, 1701912.
- [45] Y. Xiao, N. M. Abbasi, Y.-F. Zhu, S. Li, S.-J. Tan, W. Ling, L. Peng, T. Yang, L. Wang, X.-D. Guo, Y.-X. Yin, H. Zhang, Y.-G. Guo, *Adv. Funct. Mater.* **2020**, 30, 2001334.
- [46] J. Naumann, N. Bohn, O. Birkholz, M. Neumann, M. Müller, J. R. Binder, M. Kamlah, *Batteries & Supercaps* **2023**, 6, 202300264.
- [47] H. Geßwein, P. Stübke, D. Weber, J. R. Binder, R. Mönig, *J. Appl. Crystallogr.* **2022**, 55, 503.